Optics Letters

Highly efficient detection of near-infrared optical vortex modes with frequency upconversion

Yujia Wu,[1] Haigang Liu,[1,4] and Xianfeng Chen[1,2,3,5]

[1]State Key Laboratory of Advanced Optical Communication Systems and Networks, School of Physics and Astronomy, Shanghai Jiao Tong University, Shanghai 200240, China
[2]Shanghai Research Center for Quantum Sciences, Shanghai 201315, China
[3]Collaborative Innovation Center of Light Manipulations and Applications, Shandong Normal University, Jinan 250358, China
[4]e-mail: liuhaigang@sjtu.edu.cn
[5]e-mail: xfchen@sjtu.edu.cn

Received 2 March 2022; revised 12 April 2022; accepted 18 April 2022; posted 18 April 2022; published 4 May 2022

Vortex beams carrying orbital angular momentum (OAM) have been widely applied in optical manipulations, optical micromachining, and high-capacity optical communications. Vortex mode detection is very important in various applications. However, the detection of near-infrared vortex modes is still difficult because of the wavelength limitations of the detection device. Here, we present a study on measuring optical near-infrared vortex modes with frequency upconversion, which can convert a near-infrared beam into a visible beam. In our experiment, the optical near-infrared vortex modes can be measured by the number and orientation of the fringes of the second harmonic intensity patterns. The proposed method is a convenient and flexible way to measure the different OAM of vortex beams, which may have potential applications in all kinds of circumstances that vortex modes involve.

https://doi.org/10.1364/OL.457462

The angular momentum of light can be divided into spin angular momentum (SAM) and orbital angular momentum (OAM), which are associated with circular polarization and the spatial mode, respectively [1]. In 1992, Allen *et al.* [2] recognized that light beams with a helix phase dependence of an azimuthal phase term $\exp(il\varphi)$ carry an OAM of $l\hbar$ per photon, where l is the topological charge (TC) or the eigenvalue of the OAM and φ refers to the azimuth angle. The light beams carrying the OAM are characterized by a donut-shaped intensity distribution, which is also known as vortex beams [3].

In addition to the amplitude, polarization, and wavelength, the OAM can be regarded as a new degree of freedom of light waves [4–6]. Vortex beams carrying OAM have been widely applied in many fields, such as optical manipulation [7,8], quantum information [9,10], free-space optical communications [11,12], and so on [13–15]. Because of the orthogonality between different OAM modes, they can be superimposed to enhance information capacity [16,17]. Moreover, OAM holography has the potential to achieve high-capacity security storage [18,19].

Since there are many useful applications of such OAM, measuring the OAM of vortex beams has become a task of great significance. There have been many methods to measure the OAM of vortex beams based on the interference method [20–22], diffraction method [23,24], geometric coordinate transformation [25,26], deep learning [27], and surface plasmon polaritons [28,29]. Over the past years, research on vortex beams has extended to near-infrared vortex beams, especially in optical communication [30]. Compared with traditional visible OAM beams, near-infrared OAM beams have many advantages, such as low loss near the zero-dispersion area in silica fiber [31,32]. However, near-infrared detectors based on InGaAs have many limitations, such as low pixel sensitivity, high noise, and stringent cooling. In contrast, silicon-based detectors have good performance in the visible wavelength [33]. Recently, Liu *et al.* [34] reported a practical solution, which is online detection of near-infrared vortices using nonlinear photonic crystals (NPCs). The near-infrared vortex beams are converted to the visible region through a three-wave mixing process, while converting the vortex beams to Gaussian modes. Then the silicon-based detector in the visible wavelength is used for detection. However, this method is dependent on the structure of the NPCs, which needs complex fabrication. It is also phase-mismatched in the longitudinal direction based on Raman–Nath diffraction. Hence, a laudable goal would be to develop a flexible and efficient method to measure near-infrared vortex beams.

In this Letter, we demonstrate a highly efficient detection method to realize measuring the near-infrared vortex modes, including the sign and the magnitude, through second harmonic generation (SHG). In our experiment, the hyperbolic gradually changing period pure-phase grating (HGCP–PPG) [35] is imprinted into the homogeneous nonlinear medium by a spatial light modulator (SLM), whose function is to converse the mode between the Laguerre–Gaussian (LG) mode and the Hermite–Gaussian (HG) mode [36]. The near-infrared OAM beams with the TC varying from ±1 to ±8 are incident on the nonlinear medium. The TC of the vortex beam can be judged from the second harmonic (SH) HG-like diffraction intensity patterns captured by a silicon-based charge-coupled device (CCD) in the visible wave band. Finally, we calculate and measure the nonlinear conversion efficiency of the SHG process, which has a high nonlinear conversion efficiency.

A schematic of the experimental setup is illustrated in Fig. 1. An Nd:YAG nanosecond laser with 1064 nm wavelength and

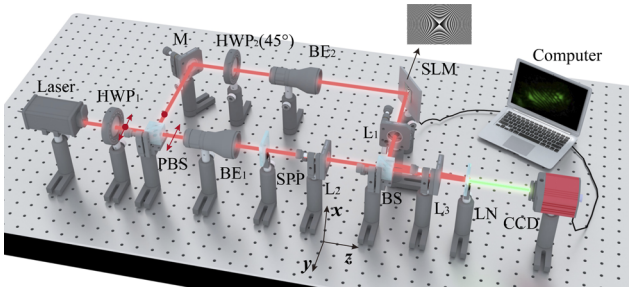

Fig. 1. Schematic of the experimental setup (see the text for details). HWP_1 and HWP_2, half-wave plates; PBS, polarization beam splitter; BE_1 and BE_2, beam expanders (2×); M, reflecting mirror; L_{1-3}, lenses, $f_{1-3} = 300$ mm, 50 mm, and 200 mm, respectively; SPP, spiral phase plate; BS, beam splitter; LN, 5 mol % MgO:$LiNbO_3$; CCD, charge-coupled device.

20 Hz repetition rate is adopted as the linearly polarized fundamental frequency (FF) wave source, which produces 4 ns pulses. A half-wave plate (HWP_1) is used to control the polarization of the FF wave. The FF wave is split into two orthogonal directions waves by a polarization beam splitter (PBS). The transmitted beam is incident on the spiral phase plate (SPP), which has an $\exp(il\varphi)$ phase distribution [2] after passing through the beam expander (BE_1). The FF wave can be expressed as follows:

$$E_1(r,\varphi) = \left(\sqrt{2}\frac{r}{\omega_0}\right)^{|l|} L_p^l\left(2\frac{r^2}{\omega_0^2}\right)\exp\left(-\frac{r^2}{\omega_0^2}\right)\exp(il\varphi), \quad (1)$$

where ω_0 is the beam waist of the FF wave, r and φ are the polar coordinates, $L_p^l(x)$ is the associated Laguerre polynomial, and p is the radial index ($p = 0$ in our experiment).

The reflected beam is incident onto a SLM (UPOLabs, HDSLM80R), which is used to load the HGCP-PPG, as illustrated in the inset of Fig. 1. The phase function of the HGCP-PPG is $\psi(x,y) = h(x^2 - y^2)$, where x and y are the Cartesian coordinates and h is a key parameter of the HGCP-PPG [35]. An additional half-wave plate (HWP_2) is inserted with its fast axis orienting at 45° to rotate the vertical polarization into the horizontal one, since the SLM is sensitive to the horizontal polarization beam. The FF wave in the SLM arm can be written as $E_2(x,y) = \exp[i\psi(x,y)]$.

The 4-f system consisting of lenses L_1 and L_3 is used to imprint the NPPG on MgO:$LiNbO_3$ (LN), while in the SPP arm, the 4-f system consisting of lenses L_2 and L_3 is used to regulate the beam size. These two beams are recombined by a beam splitter (BS) and superposed in a 10 mm × 10 mm × 1 mm 5 mol % LN to participate in the SHG process together. The LN is cut for the Type-I (oo-e) phase-matching process based on the birefringent phase matching. The angle between the propagation direction and optic axis of the crystal is 75° according to the Sellmeier equation [37]. In the non-collinear phase-matched SHG process, the intersection angle of such two FF waves is 6°, and the SH radiation angle is 80° with respect to the c axis of the crystal. Due to the small intersection angle, the two beams are approximately collinear in the thin LN. The generated SH beam can be expressed as follows:

$$E_{SH}(x,y) = A_0 L E_1(r,\varphi) E_2(x,y), \quad (2)$$

where $E_{SH}(x,y)$ represents the generated SH beam, A_0 is a parameter that characterizes the strength of the nonlinearity, and L is the thickness of the nonlinear crystal along the propagation direction. Finally, in order to get the SH patterns in the far field, the complex amplitude distribution can be recorded by the CCD, which can be written as follows:

$$E(u,v) = \frac{\exp(ikz_0)}{i\lambda z_0}\exp\left[i\frac{k}{2z_0}(u^2+v^2)\right]\cdot \int\int_{-\infty}^{\infty} E_{SH}(x,y)\exp\left(-\frac{i2\pi(ux+vy)}{\lambda z_0}\right)dxdy, \quad (3)$$

where u and v are the far-field coordinates, $E(u,v)$ is the far-field complex amplitude, λ is the FF wavelength, $k = 2\pi/\lambda$ is the wavenumber, and z_0 is the distance between the LN and the CCD ($z_0 = 500$ mm in our experiment).

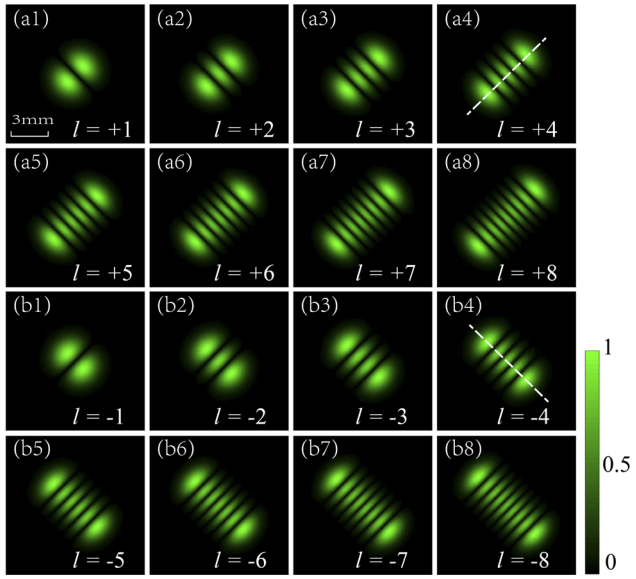

Fig. 2. Numerical simulation results of the SH intensity distribution patterns: (a1)–(a8) and (b1)–(b8) are the simulation results of the SH intensity distribution for the FF wave with TCs from $l = +1$ to $l = +8$ and $l = -1$ to $l = -8$, respectively.

The numerical simulation results are shown in Fig. 2. Figures 2(a1)–2(a8) and 2(b1)–2(b8) are the simulation results of the SH intensity distribution for the FF wave with TCs from $l = +1$ to $l = +8$ and $l = -1$ to $l = -8$, respectively. The waist of the FF wave $\omega_0 = 0.8$ mm and the optimal parameter $h = 1/\omega_0^2$ are used in the simulation. For the sake of simplicity, the FF OAM wave is vertically incident on the center of the NPPG. As shown in Fig. 2, the intensity patterns of the SH are composed of several bright spots and dark fringes, which are the HG-like light spots. With the number of TCs increasing, the value of the fringes is also increasing. Assuming that the number of bright spots is m, the TC value of the FF OAM wave is equal to $m - 1$. Meanwhile, the positive and negative TCs can be distinguished by the SH intensity distribution patterns with different orientations. For example, the orientation of the dark fringe is 45° in Fig. 2(a1), corresponding to the positive TC, while the fringe along - 45° shown in Fig. 2(b1) corresponds to negative TC.

The corresponding experiment results for measuring the TCs of the FF OAM wave from $l = +1$ to $l = +8$ and $l = -1$ to $l = -8$ are, respectively, presented in Figs. 3(a1)–3(a8) and 3(b1)–3(b8). The beam waist ω_0 is also used at about 0.8 mm in the experiment. The FF Gaussian wave at 1064 nm is incident onto the SPPs with the TC from $l = -8$ to $l = +8$. As shown in

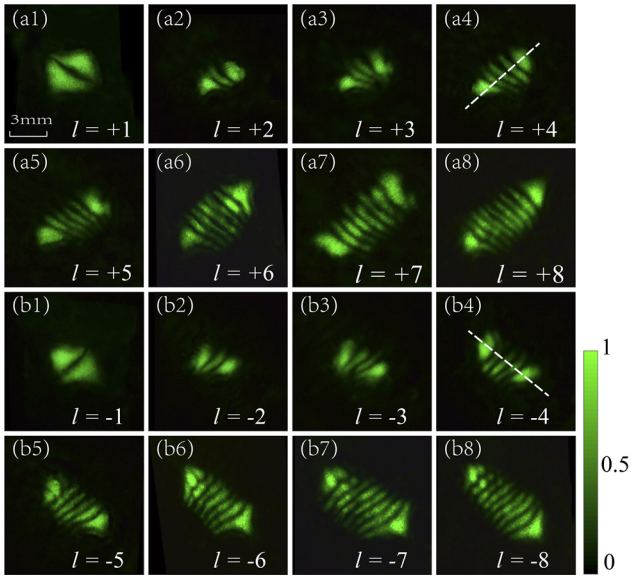

Fig. 3. Experimental results of the SH intensity distribution patterns: (a1)–(a8) and (b1)–(b8) are the measured OAM results of the SH intensity distribution for the FF OAM wave with TCs from $l = +1$ to $l = +8$ and $l = -1$ to $l = -8$, respectively.

Figs. 3(a1)–3(a8), the SH intensity distribution patterns with a visible green color are in good agreement with the numerical simulation ones. The magnitude of the TC is determined by the number of bright spots or dark fringes, which is equal to $m - 1$. The sign of the TC is distinguished by the orientation of the dark fringes. The experiment results of negative TCs are shown in Figs. 3(b1)–3(b8), in which the orientation of positive TC patterns rotates by 90° in the vertical direction. They are also in good agreement with the theoretical simulations shown in Figs. 2(b1)–2(b8). Therefore, the method we proposed enables the visualization of invisible near-infrared vortex light based on the observation of SH intensity distribution patterns.

Without loss of generality, we choose TCs of $l = 4$ and $l = -4$ to compare the theoretical and experimental intensity distribution results. The directions of the intensity distribution are indicated by white dashed white lines, as shown in Figs. 2(a4), 2(b4), 3(a4), and 3(b4). The theoretical intensity distribution results of the SH patterns corresponding to $l = 4$ and $l = -4$ are shown in Figs. 4(a) and 4(b), and the experimental ones are shown in Figs. 4(c) and 4(d). The two larger peaks at two sides of the curves represent the bright spots of the SH patterns, and the secondary peaks represent the weak bright fringes. It can be observed that the number of valleys is equal to the TCs of the measured FF OAM wave, while the valleys are marked by black dots. However, the errors with respect to the experimental results may be due to the inevitable diffraction effect.

Finally, the nonlinear conversion efficiency is measured in the experiment. As shown in Fig. 5(a), the power variation of the SH beam changes with the increase of the FF power in the SPP arm as the TC is 4. The FF power in the SPP arm power is from 5.8 mW to 24 mW, while the average power of the FF wave in the SLM arm adjusted by HPW_1 is constant at 5 mW. The conversion of the SH beam is given by $\eta \propto CP_{SH}/(P_{FW_1} \cdot P_{FW_2})$, where P_{SH} is the average power of the SH wave, P_{FW_1} and P_{FW_2} are the average power of the FF wave in the SPP arm and the

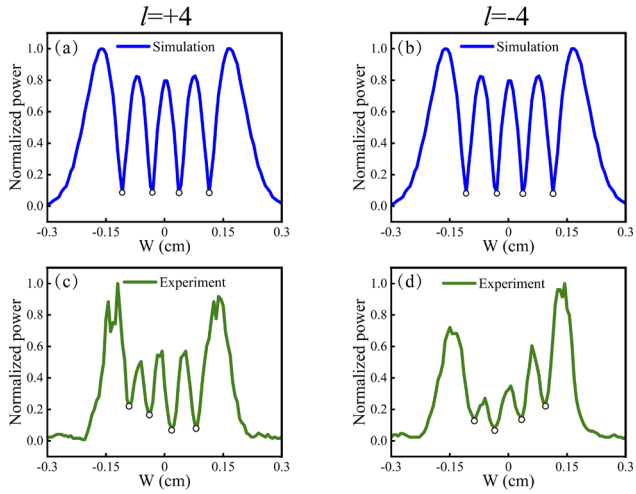

Fig. 4. Intensity distributions of the SH patterns, which are perpendicular to the bright fringes: (a), (b) the theoretical intensity distribution results; (c), (d) the measured intensity distribution results corresponding to $l = +4$ and $l = -4$, respectively. W is the distance along the fringe structure.

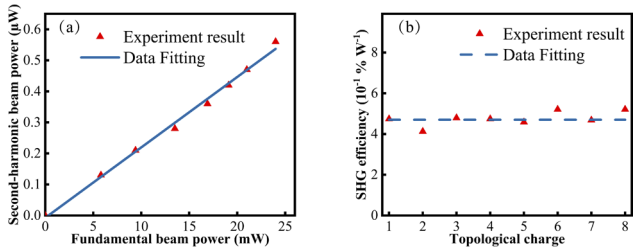

Fig. 5. (a) Comparison between measured (triangle) and linear fit (solid curves) results of the average SH beam power dependence on the average FF input power in the SPP arm. (b) SHG efficiency as the topological charge changes from 1 to 8.

SLM arm, respectively, and C is a constant. Figure 5(a) confirms a linear relation between P_{SH} and P_{FW_1}. The nonlinear conversion efficiency from the FF wave in the SLM arm and the SPP arm to the current SH beam is about $4.7 \times 10^{-1}\%W^{-1}$ in the case of $l = 4$. Further, we measured the SHG efficiency as the TC changes from 1 to 8, as shown in Fig. 5(b). The FF wave power in the SPP arm is about 9.7 mW, which is basically unchanged with the variations of TCs. Obviously, with the increase of TC, the conversion efficiency of the SH generation is about $4.7 \times 10^{-1}\%W^{-1}$, while the dashed line represents $4.7 \times 10^{-1}\%W^{-1}$. While the TC is increasing, the OAM radius is basically unchanged because the beam size is compressed by the 4-f system in the SPP arm. Therefore, the overlapping energy of the two beams is basically constant and the efficiency is almost unchanged.

In our experiment, the HGCP–PPG is used to realize such near-infrared vortex mode detection, since it has been proved to have excellent properties by Liu *et al.* [35]. We would like to point out that the method that we proposed can be used to measure an unbounded OAM state without redesigning the structure of the nonlinear material. For different FF beam waists, it is convenient to get the measured OAM result by updating the loaded HGCP–PPG onto the SLM. Moreover, it has a relatively high conversion efficiency based on the phase-matched SHG process,

which can be achieved with nanosecond beams compared with the method of Liu *et al.* [34]. It can also be used for online detection of high-energy classical beams because the non-collinear process does not change the vortex mode.

In conclusion, we have realized a highly efficient method to measure optical near-infrared vortex modes with frequency upconversion, which is determined by the direction and number of dark fringes of the measured SH HG-like diffraction patterns. In our experiment, we have measured the OAM near-infrared beams with TCs from $l = \pm 1$ to $l = \pm 8$. The experimental results agree well with the simulations. In addition, the relationship between the power of the SH beam and the FF beam in the SPP arm is studied. The result indicates that the power of SH beam varied linearly with the FF beam in the SPP arm. This method may have potential in optical communication or fiber optics, where near-infrared vortex modes are expected to be measured.

Funding. National Key Research and Development Program of China (2017YFA0303701, 2018YFA0306301); National Natural Science Foundation of China (11734011, 12004245, 12074252, 62022058); Shanghai Municipal Science and Technology Major Project (2019SHZDZX01-ZX06); Shanghai Rising-Star Program (20QA1405400); Startup Fund for Young Faculty at SJTU (21X010500780); China Postdoctoral Science Foundation (2021M692095).

Disclosures. The authors declare no conflicts of interest.

Data availability. Data underlying the results presented in this paper are not publicly available at this time but may be obtained from the authors upon reasonable request.

REFERENCES

1. D. L. P. Vitullo, C. C. Leary, P. Gregg, R. A. Smith, D. V. Reddy, S. Ramachandran, and M. G. Raymer, Phys. Rev. Lett. **118**, 083601 (2017).
2. L. Allen, M. W. Beijersbergen, R. J. C. Spreeuw, and J. P. Woerdman, Phys. Rev. A **45**, 8185 (1992).
3. D. Gauthier, P. R. Ribic, G. Adhikary, A. Camper, C. Chappuis, R. Cucini, L. F. Dimauro, G. Dovillaire, F. Frassetto, R. Géneaux, P. Miotti, L. Poletto, B. Ressel, C. Spezzani, M. Stupar, T. Ruchon, and G. De Ninno, Nat. Commun. **8**, 14971 (2017).
4. J. Wang, J. Y. Yang, I. M. Fazal, N. Ahmed, Y. Yan, H. Huang, Y. Ren, Y. Yue, S. Dolinar, M. Tur, and A. E. Willner, Nat. Photonics **6**, 488 (2012).
5. N. Bozinovic, Y. Yue, Y. Ren, M. Tur, P. Kristensen, H. Huang, A. E. Willner, and S. Ramachandran, Science **340**, 1545 (2013).
6. J. Liu, S. M. Li, L. Zhu, A. D. Wang, S. Chen, C. Klitis, C. Du, Q. Mo, M. Sorel, S. Y. Yu, X. L. Cai, and J. Wang, Light: Sci. Appl. **7**, 17148 (2018).
7. M. Padgett and R. Bowman, Nat. Photonics **5**, 343 (2011).
8. M. Gecevičius, R. Drevinskas, M. Beresna, and P. G. Kazansky, Appl. Phys. Lett. **104**, 231110 (2014).
9. A. Nicolas, L. Veissier, L. Giner, E. Giacobino, D. Maxein, and J. Laurat, Nat. Photonics **8**, 234 (2014).
10. R. Fickler, Science **338**, 640 (2012).
11. Y. Yan, Y. Yue, H. Huang, Y. Ren, N. Ahmed, M. Tur, S. Dolinar, and A. Willner, Opt. Lett. **38**, 3930 (2013).
12. A. E. Willner, H. Huang, Y. Yan, Y. Ren, N. Ahmed, G. Xie, C. Bao, L. Li, Y. Cao, Z. Zhao, J. Wang, M. P. J. Lavery, M. Tur, S. Ramachandran, A. F. Molisch, N. Ashrafi, and S. Ashrafi, Adv. Opt. Photonics **7**, 66 (2015).
13. L. Huang, X. Chen, H. Mühlenbernd, G. Li, B. Bai, Q. Tan, G. Jin, T. Zentgraf, and S. Zhang, Nano Lett. **12**, 5750 (2012).
14. X. Pan, S. Yu, Y. Zhou, K. Zhang, K. Zhang, S. Lv, S. Li, W. Wang, and J. Jing, Phys. Rev. Lett. **123**, 070506 (2019).
15. P. Georgi, C. Schlickriede, G. Li, S. Zhang, and T. Zentgraf, Optica **4**, 1000 (2017).
16. I. B. Djordjevic, Opt. Express **19**, 14277 (2011).
17. Q. Zhao, P. P. Yu, Y. F. Liu, Z. Q. Wang, Y. M. Li, and L. Gong, Appl. Phys. Lett. **116**, 181101 (2020).
18. X. Fang, H. Ren, and M. Gu, Nat. Photonics **14**, 102 (2020).
19. H. Zhou, B. Sain, Y. Wang, C. Schlickriede, R. Zhao, X. Zhang, Q. Wei, X. Li, L. Huang, and T. Zentgraf, ACS Nano **14**, 5553 (2020).
20. H. I. Sztul and R. R. Alfano, Opt. Lett. **31**, 999 (2006).
21. Q. Zhao, M. Dong, Y. Bai, and Y. Yang, Photonics Res. **8**, 745 (2020).
22. J. Leach, M. J. Padgett, S. M. Barnett, S. Franke-Arnold, and J. Courtial, Phys. Rev. Lett. **88**, 257901 (2002).
23. J. M. Hickmann, E. J. S. Fonseca, W. C. Soares, and S. Chávez-Cerda, Phys. Rev. Lett. **105**, 053904 (2010).
24. K. Dai, C. Gao, L. Zhong, Q. Na, and Q. Wang, Opt. Lett. **40**, 562 (2015).
25. Y. Guo, S. Zhang, M. Pu, Q. He, J. Jin, M. Xu, Y. Zhang, P. Gao, and X. Luo, Light: Sci. Appl. **10**, 63 (2021).
26. Y. Wen, I. Chremmos, Y. Chen, J. Zhu, Y. Zhang, and S. Yu, Phys. Rev. Lett. **120**, 193904 (2018).
27. Z. Liu, S. Yan, H. Liu, and X. Chen, Phys. Rev. Lett. **123**, 183902 (2019).
28. J. Chen, X. Chen, T. Li, and S. Zhu, Laser Photonics Rev. **12**, 1700331 (2018).
29. F. Feng, G. Si, C. Min, X. Yuan, and M. Somekh, Light: Sci. Appl. **9**, 95 (2020).
30. X. Fang, H. Yang, W. Yao, T. Wang, Y. Zhang, M. Gu, and M. Xiao, Photonics **3**, 015001 (2021).
31. E. Agrell, M. Karlsson, A. R. Chraplyvy, D. J. Richardson, P. M. Krummrich, P. Winzer, K. Roberts, J. K. Fischer, S. J. Savory, B. J. Eggleton, M. Secondini, F. R. Kschischang, A. Lord, J. Prat, I. Tomkos, J. E. Bowers, S. Srinivasan, M. Brandt-Pearce, and N. Gisin, J. Opt. **18**, 063002 (2016).
32. H. Ren, X. Li, Q. Zhang, and M. Gu, Science **352**, 691 (2016).
33. A. Rogalski, Infrared Phys. Technol. **43**, 187 (2002).
34. Y. Liu, W. Chen, W. Zhang, C. Q. Ma, H. X. Chen, Y. F. Xiong, R. Yuan, J. Tang, P. Chen, W. Hu, F. Xu, and Y. Q. Lu, Adv. Opt. Mater. **10**, 2101098 (2022).
35. Z. Liu, S. Gao, W. Xiao, J. Yang, X. Huang, Y. Feng, J. Li, W. Liu, and Z. Li, Opt. Lett. **43**, 3076 (2018).
36. E. Abramochkin and V. Volostnikov, Opt. Commun. **83**, 123 (1991).
37. O. Gayer, Z. Sacks, E. Galun, and A. Arie, Appl. Phys. B: Lasers Opt. **91**, 343 (2008).